Geometric Strategies for Neuroanatomic Analysis from MRI

James S. Duncan [a,b,c], Xenophon Papademetris [a,b], Jing Yang [c], Marcel Jackowski [a], Xiaolan Zeng [c], and Lawrence H. Staib [a,b,c]

[a] *Departments of Diagnostic Radiology,*

[b] *Biomedical Engineering and*

[c] *Electrical Engineering, Yale University, New Haven, CT, USA*

Abstract

In this paper, we describe ongoing work in the Image Processing and Analysis Group (IPAG) at Yale University specifically aimed at the analysis of structural information as represented within magnetic resonance images (MRI) of the human brain. Specifically, we will describe our applied mathematical approaches to: the segmentation of cortical and subcortical structure, the analysis of white matter fiber tracks using diffusion tensor imaging (DTI) and the intersubject registration of neuroanatomical (aMRI) datasets. Many of our methods rally around the use of geometric constraints, statistical (MAP) estimation and the use of level set evolution strategies. The analysis of gray matter structure and connecting white matter paths combined with the ability to bring all information into a common space via intersubject registration should provide us with a rich set of data to investigate structure and variation in the human brain in neuropsychiatric disorders, as well as provide a basis for current work in the development of integrated brain function/structure analysis.

1 Introduction

Accurate and robust extraction and measurement of neuroanatomic structure in the human brain from magnetic resonance images remains a challenging area of research. Within the Image Processing and Analysis Group (IPAG) at Yale University, we have been developing mathematical approaches to aspects of this problem, with a focus on using appropriate geometrical and statistical constraints and decision-making strategies for particular subproblems in the domain. We have identified four key areas important to our efforts, each of which requires a unique approach: 1.) the segmentation and measurement

of cortical gray matter structure, 2.) the segmentation and measurement of subcortical gray matter structure, 3.) tracking and analysis of white matter fiber pathways and 4.) structurally-focused intersubject image registration for developing multisubject measures. There are, of course, other processing issues in the analysis of human brain images, such as bias field correction, that are not discussed here. Methods for the analysis of subcortical gray matter, cortical gray matter and white matter combined with intersubject registration techniques provide the foundation for detailed investigation of brain structure in neuropsychiatric disorders. These structural methods also provide the basis for our ongoing research of integrated brain function/structure analysis techniques. In this section, we present related work in each area and describe our own efforts in the ensuing sections.

Cortical Image Segmentation Work in segmenting the cortex from 3D MR images has fallen into two broad categories: voxel classification and deformable models. Classifying gray and white matter by voxel intensity can incorporate voxel continuity or homogeneity using, for example, Markov random fields [1,2] to model probabilistic constraints on the image or fuzzy logic [3]. The approach of Wells *et al.* [4] estimates tissue classes (gray matter, white matter, cerebrospinal fluid - CSF) while simultaneously estimating the bias field using an expectation-maximization (EM) strategy. Cline *et al.* [5] use multispectral voxel classification in conjunction with connectivity to segment the brain into tissue types. Material mixture models [6] have also been used. Region-based methods of this type typically require further processing to group segmented regions into coherent structures.

Snakes or Active Contour Models (ACM) [7] are energy minimizing parametric contours with smoothness constraints. Unlike level set implementations [8,9], the direct implementation of this energy model is not capable of handling topological changes of the evolving contour without explicit discrete model parameter manipulations. Deformable models using level set methods [10–12] analyze and compute interface motion representing the boundary as a propagating wavefront. Level set methods are quite powerful and have useful properties of topologic flexibility. They need to be carefully constrained in order to avoid stopping short or flowing too freely beyond the desired boundaries. Methods have been devised to preserve topology when necessary [13]. See below for further discussion of level set methods.

Deformable models specifically tailored for segmenting the cortical gray matter have been devised. Davatzikos *et al.* [14] proposed an active contour algorithm for determining the spine of a ribbon modeling the outer cortex. Xu *et al.* [15] use gradient vector flow fields in conjunction with tissue membership to control the deformation of active contour models for finding the central gray matter layer. Teo *et al.* [16] designed an approach in which white matter

and CSF regions were first segmented, followed by connectivity analysis and a constrained deformation from the white matter boundary. MacDonald *et al.* [17] simultaneously deform multiple surfaces to segment the brain using multiple cost function constraint terms. This approach takes advantage of the information of the interrelation between the surfaces of interest, but is computationally expensive with many parameters to tune. Kapur *et al.* [18] also use a snake approach, in conjunction with EM segmentation and mathematical morphology. Unlike subcortical structure (discussed below), the cortex is highly variable and thus generally not well suited for specific prior shape models [19] unless limited to specific regions of the cortex; more generic constraints are necessary. In work we describe in more detail in the next section, Zeng *et al.* [20] developed a coupled level set algorithm to segment the cortex using a geometric constraint based on the consistency of cortical thickness.

Once the cortical layers are segmented a variety of useful neuroanatomical measurement parameters can be derived. Examples of these include sulcal depth, cortical thickness and/or cortical shape (e.g. [21,22]). In the work of Vaillant *et al.* [21], special "ribbon" operators were developed to characterize the depth of the sulcal grooves. A related example is the automated extraction of sulcal and gyral curves using crest lines from the differential geometric properties of a segmented brain surface [23]. The extraction of shape features from a segmented anatomical object in this way may be useful not only for measurement but feature-based registration as well.

Subcortical Structure Segmentation Statistical models can be powerful tools to directly capture the variability of structures being modelled. Such techniques are a necessity for the segmentation of subcortical structure which have consistent shape but are poorly defined by image features. Atlas registration for the purposes of segmentation [24,25] is one way of using prior shape information. Collins *et al.* [26], for example, segment the brain using an elastic registration to an average brain, based on a hierarchical local correlation. The average brain provides strong prior information about the expected image data and can be used to form probabilistic brain atlases [27,26]. Specific models for prior shape have been used successfully in our lab [28–32] and by other groups [33,34] for segmentation. The statistics of a sample of images can be used to guide the deformation in a way governed by the measured variation of individuals. Region-based information can also be combined with prior models [35–37] in order to enhance robustness.

Level set methods and new energy terms have been reported to increase the capture range of deformable models and incorporate prior shape information. Chan and Vese [38] proposed a level set method that can detect objects whose boundaries are not necessarily defined by gray level gradients. Leventon *et al.* [39] extended Caselles' [40] geodesic active contours by incorporating shape

information into the evolution process. In our work, described in this paper, we adopt a level set approach using prior information of the shape of an object and its neighbors [31,41]. We note that Tsai *et al.* describe a similar approach [42,43] which uses a global multi-shape model. We feel that our approach is more flexible in the modeling of joint priors and accommodates situations with limited inter-object information and variation in contrast and discernibility among the objects.

Typically, the accurate and meaningful measurement of normal and abnormal subcortical structure includes volume, surface area as well as shape measures. These analysis methods require processing beyond the initial steps of segmentation and/or registration of datasets [44].

Analysis of White Matter Fiber Tracks Using Diffusion Tensor Imaging While the basic anatomy of white matter tracts in the human brain is generally known from anatomical dissection, much is unknown about its interconnections and its natural variations. The characterization and quantitative measurement of its connections is of fundamental importance in understanding brain function. Diffusion Tensor Magnetic Resonance Imaging (DT-MRI) has emerged as a noninvasive imaging modality capable of providing this information *in vivo*, enabling the detailed study of white matter structure in the human brain.

Brain white matter, because of the long and fibrous nature of axons, exhibits higher restriction to water diffusion across the fibers than along them. This directional variation is measured in diffusivity rates and can be captured by diffusion-weighted MRI. By acquiring diffusion-weighted data in at least six non-collinear directions, it is possible to estimate a 3×3 symmetric matrix (i.e. diffusion tensor) which characterizes diffusion in anisotropic systems [45]. After tensor diagonalization, the eigenvector corresponding to the largest eigenvalue is considered to point along the direction of a fiber bundle.

Many connectivity studies relying on the straightforward integration of the principal tensor eigenvector have been described in the literature [46]. Their reliability, however, is limited by acquisition noise and partial voluming due to fiber tracts that cross, branch and merge. To account for these variations, level set methods [47] have been employed (e.g. [48–50]). These techniques model the evolution of an advancing front through the white matter tracts by following the local directionality provided by the diffusion tensor field. Such methods have been shown to be more robust to noise and singularities than classical streamlining methods. A tractography technique based on the fast marching method (FMM) was used by Parker *et al.* [48]. A front was evolved with a speed proportional to the collinearity between the front normal and the principal tensor eigenvector. A discrete approximation of front direction

had to be used to drive the evolution through the eigenvector field, since the original FMM cannot handle propagation in oriented domains. Others have posed the connectivity problem in a Riemannian framework (e.g. [50,49]).

As will be described later, in our group, we have developed a novel wavefront propagation method for estimating the connectivity in the white matter of the brain using DT-MRI.

Image Registration/Matching In order to gain statistical power for comparing groups of subjects in either structural or functional brain image analysis, it can be useful to pool image information from many subjects. In these cases, a key step is the formation of multisubject composite activation maps where each subject is nonrigidly mapped to a common coordinate space. Group characterization using composite activation or structural variation maps can then be computed on a voxel-wise basis. However, nonrigid registration of brain images is a difficult task.

Previously, Talairach-type methods [51] have been used but the limitations of these methods are well known [52,53]. True nonrigid registration is necessary to bring the subjects into a common space. There have been many approaches recently to nonrigid registration, with a particular emphasis on applications to brain imaging (see the recent special journal issues [54,55]). Most commonly, nonrigid registration methods use image intensities to compute the transformation [56–58]. The high anatomic variability of the cortex can often result in intensity based methods yielding inaccurate results due to local minima, as was recently demonstrated [59]. These errors are of particular concern in functional MRI (fMRI) analysis for evaluating cortical activations.

Feature based methods have been developed to overcome the limitations of gray-level methods [60–62]. None of these methods, however, is able to handle large variations in sulcal anatomy, as well as irregular sulcal branching and discontinuity. In our work, which will be described in a later section, we extend the robust point matching (RPM) algorithm [63] to better address brain registration. We use a point matching strategy to register structurally salient regions as part of our strategy to generate higher resolution composite functional maps tailored to specific regions.

2 Coupled Level Sets for Cortical Segmentation

We have developed a coupled surfaces approach [20] to segment cortical structure. In this work, a local gray level operator designed to obtain the likelihood of each voxel lying on the outer and inner cortical surfaces respectively, is used

instead of simple gradient information. A gradient operator will respond to all gray level transitions at a given scale. By focusing on the gray-level transitions of interest, we remove extraneous information that could impede the propagation of the level sets. Key to the approach is that the surfaces representing the gray matter/white matter cortical interface (inner) and gray/CSF interface (outer) are found in an integrated manner by evolving two coupled level sets. Thus, starting from inside the inner bounding surface (gray/white boundary), with an offset in between, the interfaces propagate along the normal direction stopping at the desired location, while maintaining a distance between them.

The Basic Strategy. Embedding each surface as the zero level set in its own level function Ψ, we have two equations:

$$\begin{aligned} \Psi_{in_t} + F_{in} \mid \nabla \Psi_{in} \mid &= 0 \\ \Psi_{out_t} + F_{out} \mid \nabla \Psi_{out} \mid &= 0 \end{aligned} \tag{1}$$

where F_{in} and F_{out} are speed functions of the surface normal, image-derived information and distance between the two surfaces. The coupling is embedded in the design of F_{in} and F_{out}. Where the distance between the two surfaces is within the normal range for cortical thickness, the two surfaces propagate according to the image-based information; where the distance is out of the normal range, the distance constrains the propagation. The level set implementation provides an easy and natural way to evaluate the distance between the two surfaces because the value of the level function at any point is simply the distance from this point to the current front, which as in Sethian [12], is calculated as the shortest distance from this point to the points on the front. In our case of the two moving surfaces, for any point on the inner moving surface, the distance to the outer moving surface is the value Ψ_{out} at this point, and vice versa for the point on the outer moving surface, i.e. its distance is Ψ_{in}.

Experiments and Results. This approach has been tested on simulated data (with known underlying segmentations) created from the Montreal Neurological Institute's MR simulator [64] (using different noise conditions and 1mm^3 voxels) with very encouraging results: true positive rates greater than 92% and false positive rates less than 6% for segmentation of cortical gray matter [20]. In addition, as reported in part in Zeng *et al.* [20], we have run our coupled-surface cortical layer segmentation strategy on 20 normal brains and compared our results to known manual segmentations from the Internet Brain Segmentation Repository [65] (about $1\times1\times3$ mm^3 voxels). In this work, we were able to illustrate that our approach outperformed six other

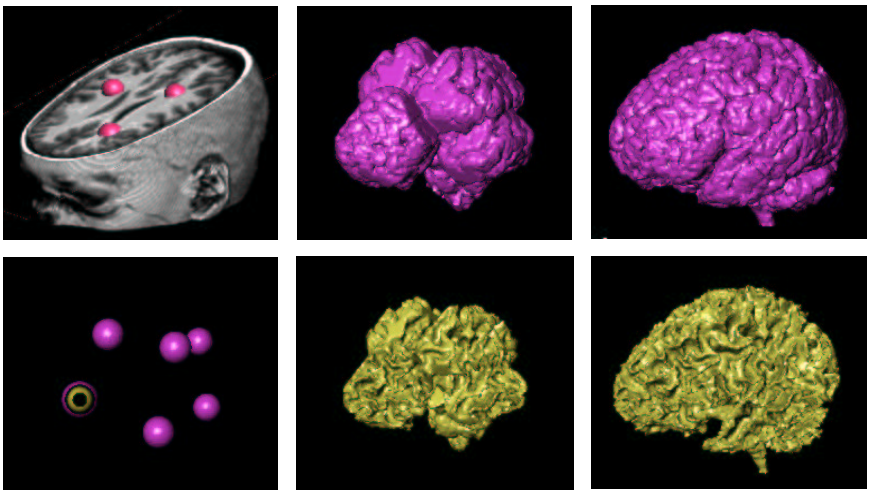

(a) (b) (c)

Fig. 1. Results of cortical gray matter segmentation using coupled level sets. (a) Initialization of pairs of concentric spheres in 3D MR brain images; (b) intermediate step; (c) final result of the outer (top) and inner (bottom) cortical surfaces of the frontal lobe. *Figure reprinted from X. Zeng, L. H. Staib, R. T. Schultz and J. S. Duncan, Segmentation and Measurement of the Cortex from 3D MR Images Using Coupled Surfaces Propagation,* IEEE Transactions on Medical Imaging, *18(10) [20],* ©1999 *IEEE, by permission from the IEEE.*

automated algorithms in the literature in terms of the average overlap with pooled-manual-expert segmentations (with 1.0 perfect and 0.0 the worst, our approach on cortical gray matter achieved 0.701, and the next best algorithm, 0.564). In addition, we have run this approach on over 60 subjects acquired on our 1.5T GE Signa system at Yale (SPGR acquisition, $(1.2\text{mm})^3$ voxels). A typical result from these data is shown in Figures 1 and 2. For one group of 14 human subjects, there was 87% true positive findings for each subject in comparison to manual tracings of the frontal cortical gray matter layer, although with false positives in the 20% range. Errors can occur where the outer cortical surface is obscured, such as due to susceptibility artifacts in the orbital frontal cortex.

This approach provided the basis for further processing of sulcal features ("ribbons") to quantify sulcal depth and shape [66] (see Figure 3).

3 Neighbor-constrained Subcortical Segmentation

We have developed a novel method for the segmentation of multiple objects from 3D medical images using inter-object constraints, that we have employed as our subcortical structure segmentation strategy [67,68,32,31]. Our method

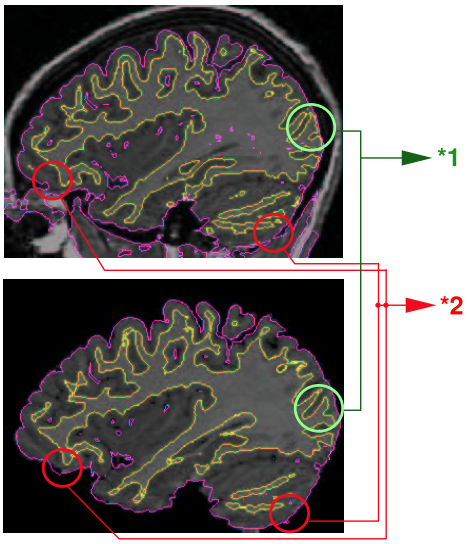

Fig. 2. Single vs. coupled surfaces approach. Top: surfaces resulting from finding the inner and outer cortex separately, shown on a sagittal slice through the 3D result. Bottom: results from the coupled surfaces approach run on original 3D data overlaid on a sagittal slice of the expert tracing result. The outer cortical surface resulting from the coupled algorithm nicely fits the boundary from the expert tracing. Coupling prevents the inner surface from collapsing into CSF(*1) and the outer surface from penetrating non-brain tissue(*2). *Figure reprinted from X. Zeng, L. H. Staib, R. T. Schultz and J. S. Duncan, Segmentation and Measurement of the Cortex from 3D MR Images Using Coupled Surfaces Propagation,* IEEE Transactions on Medical Imaging, *18(10) [20],* ©1999 *IEEE, by permission from the IEEE.*

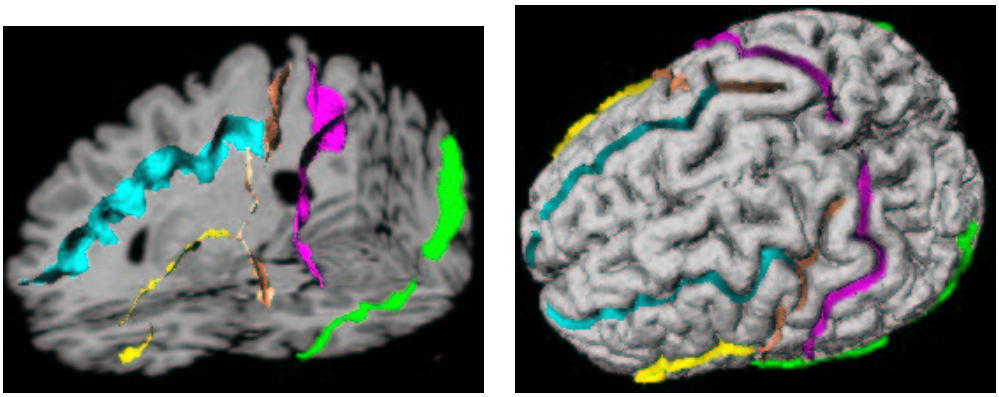

(a) (b)

Fig. 3. Sulcal surfaces ("ribbons") shown (a) with cut-away view of brain and (b) on outer cortical rendering. *Figure reprinted from X. Zeng, L. H. Staib, R. T. Schultz, H. Tagare, L. Win and J. S. Duncan, A New Approach to 3D Sulcal Ribbon Finding from MR Images, in* Medical Image Computing and Computer-Assisted Intervention, *1999. LNCS 1679. [66],* ©1999 *by permission from Springer-Verlag.*

is motivated by the observation that neighboring structures have consistent locations and shapes that provide configurations and context that aid in segmentation. In this effort, we have defined a *maximum a posteriori* (MAP) estimation framework using the constraining information provided by neighboring objects to segment several objects simultaneously. Within the MAP strategy, we assume that the likelihood (data-adherence) term and the prior term are Gaussian. The segmented surface can be found using discrete approximations to level set functions, and computing the associated Euler-Lagrange equations. The contours evolve both according to prior information related to the shape of the object of interest and relational shape and position information, as well as the image gray level information. We have recently compared [41] these level-set-based shape models with point-based models, and have been able to show that the priors formed from either method are not statistically different for the test shapes examined, although the level set approach can accommodate varying topology, a notion that we intend to ultimately exploit in our work. These methods are useful in situations where there is limited inter-object information as opposed to robust global atlases.

The MAP framework Relating the development from Yang *et al.* [67], but recasting the notation slightly, we describe our approach as follows. Consider a structural image represented as a random field $\mathbf{I}$ that has $i = 1, \ldots, M$ structures of interest. Next assume that the boundary of each object i can be embedded as the zero level set of a 3D (Euclidean) distance function Ψ_i. These distance functions can be sampled yielding discrete 3D versions for each structure of interest $S_i,\ i = 1, \ldots, M$. Furthermore, we can model the distributions of shape, size and position of any structure i by assuming $\mathbf{S_i}$ to be a random field (rf) and then measuring instances of each rf over a number of subjects, thereby constructing the probability density functions (pdfs) $p(\mathbf{S_i})$.

Each outcome of $\mathbf{S_i}$ is represented by an N^3-long column vector that is a row-by-row stacking of the matrix found by discretely sampling the corresponding level set distance function Ψ_i in the image space. We have shown [68], that the level set distance function of any one object $\mathbf{S_i}$ that depends on its neighbors can be estimated using the following MAP framework:

$$\begin{aligned} \hat{S}_i &= \arg\max_{\mathbf{S_i}} p(\mathbf{S_1}, \mathbf{S_2}, \cdots, \mathbf{S_i}, \cdots, \mathbf{S_M} | \mathbf{I}) \\ &= \arg\max_{\mathbf{S_i}} p(\mathbf{I} | \mathbf{S_1}, \mathbf{S_2}, \cdots, \mathbf{S_i}, \cdots, \mathbf{S_M}) p(\mathbf{S_1}, \mathbf{S_2}, \cdots, \mathbf{S_i}, \cdots, \mathbf{S_M}), \end{aligned} \tag{2}$$

for $i = 1, 2, \cdots, M$ and where $p(\mathbf{I}|\mathbf{S_1}, \mathbf{S_2}, \cdots, \mathbf{S_M})$ is the probability of producing an image $\mathbf{I}$ given $\mathbf{S_1}$, $\mathbf{S_2}$, $\cdots$, $\mathbf{S_M}$. In 3D, assuming gray level homogeneity within each object, we implemented the following image-data term (adapted from Chan and Vese [38]):

$$p(\mathbf{I}|\mathbf{S_1}, \mathbf{S_2}, \cdots, \mathbf{S_M}) = \prod_{i=1}^{M} \left\{ \prod_{(x,y,z) inside(\mathbf{S_i})} e^{-\frac{(I(x,y,z)-c_{1i})^2}{2\sigma_{1i}^2}} \prod_{(x,y,z) outside(\mathbf{S_i}), inside(\Omega_i)} e^{-\frac{(I(x,y,z)-c_{2i})^2}{2\sigma_{2i}^2}} \right\} \quad (3)$$

where c_{1i} and σ_{1i} are the average and variance of $\mathbf{I}$ inside the zero level set of $\mathbf{S_i}$. c_{2i} and σ_{2i} are the average and variance of $\mathbf{I}$ outside the zero level set of $\mathbf{S_i}$ but within a domain Ω_i that contains $\mathbf{S_i}$. In our work, we typically set the domain Ω_i to be where the level set distance is no more than the average diameter of the object of interest.

Furthermore, $p(\mathbf{S_1}, \mathbf{S_2}, \cdots, \mathbf{S_M})$ is the joint density function of all the M objects. It contains neighbor prior information such as the relative position and shape among the objects. A variety of relational assumptions can be used here, but in situations where the neighbors are sometimes difficult to locate, we initially assumed that each object is related to the key object (denoted object k) independently. In this case, the joint density function can be simplified to:

$$\begin{aligned} p(\mathbf{S_1}, \mathbf{S_2}, \cdots, \mathbf{S_M}) &= p(\mathbf{S_M}|\mathbf{S_k}) \cdots p(\mathbf{S_2}|\mathbf{S_k}) p(\mathbf{S_k}) = \\ &= p(\mathbf{\Delta_{M,k}}) p(\mathbf{\Delta_{M-1,k}}) \cdots p(\mathbf{\Delta_{2,k}}) \mathbf{p}(\mathbf{S_k}) \end{aligned} \quad (4)$$

where $\mathbf{\Delta_{jk}} = p(\mathbf{S_j}|\mathbf{S_k}) = \mathbf{S_j} - \mathbf{S_k}$ is the difference between the level sets of object j and k. The process of defining the joint density function $p(\mathbf{S_1}, \mathbf{S_2}, \cdots, \mathbf{S_M})$ is simplified to building only the self prior, $p(\mathbf{S_k})$, and the local neighbor priors $p(\mathbf{\Delta_{jk}}), j, k = 1, 2, \cdots, M;\ j \neq k$.

Consider a training set of n aligned images, with M objects or structures in each image. As described above, each object i in the training set is embedded as the zero level set of a higher dimensional level set Ψ_i whose discretized distance function is the N^3 column vector $\mathbf{S_i}$. As in our previous efforts in the estimation of the segmentation of a single object in an image (e.g. [28,37]), we deem it important to first be able to model the range of plausible object self-shape information. Here, we assume that the shapes vary smoothly in a relatively compact portion of a high dimensional manifold such that we can model their variation using Principal Component Analysis (PCA). Thus, the pdf of the level function of object i can be computed using PCA similar to what is done for point distribution models [33]. An estimate of $\mathbf{S_i}$ can be represented by the mean level set $\bar{\mathbf{S}}_\mathbf{i}$, p principal components U_i and a p dimensional vector of coefficients (where $p < n$), α_i: $\tilde{\mathbf{S}}_i = U_i \alpha_i + \bar{\mathbf{S}}_i$. Under the assumption of a Gaussian distribution of shape represented by α_i, we can compute the probability of object i: $p(\alpha_i) = \mathcal{N}(0, \Sigma)$.

The level set representation of shape provides tolerance to slight misalign-

ment of object shape, in an attempt to avoid having to solve the general correspondence problem. In practice, the variations captured by the principal components in the level set distribution model (U_i) in this paper are based on a rigid alignment of the training data and may contain undesired residuals due to misalignment. We are looking to improve the alignment method in order to reduce such residuals and undesired topology changes.

Due to the assumptions in our initial work above, i.e. that each neighbor is independently related to the object of interest, we can use the difference between the two level sets, $\mathbf{S_j} - \mathbf{S_k}$, as the representation of the neighbor difference $\mathbf{\Delta_{jk}}, j = 1, 2, 3, \cdots, M$ shown above (this implicitly represents $\mathrm{P}(\mathbf{S_j}|\mathbf{S_k})$ We again assume that the distribution of $\mathbf{\Delta_{jk}}$'s for any key object k form a compact portion of a high dimensional space such that the distribution can be parameterized using a linear PCA formulation. Thus, the range of neighbor-to-object variation for each object can be found from the mean neighbor difference $\bar{\mathbf{\Delta}}_{\mathbf{jk}}$ and p principal components P_{jk} and a p dimensional vector of coefficients, β_{jk}: $\tilde{\mathbf{\Delta}}_{jk} = P_{jk}\beta_{jk} + \bar{\mathbf{\Delta}}_{jk}$. We assume the neighbor difference $\mathbf{\Delta}_{jk}$ to be Gaussian distributed over β_{jk}: $p(\beta_{jk}) = \mathcal{N}(0, \Lambda_{jk})$.

Using the techniques described in Chan and Vese [38], we compute the associated Euler-Lagrange equation for each unknown level set function (written here for convenience in terms of the continuous functions Ψ_k):

$$\begin{aligned}\frac{\partial \Psi_k}{\partial t} = &\delta_\varepsilon(\Psi_k)\left[\mu_k \cdot \mathrm{div}\left(\frac{\nabla \Psi_k}{|\nabla \Psi_k|}\right) + \nu_k + \lambda_{1k}|I - c_{1k}|^2 - \lambda_{2k}|I - c_{2k}|^2\right] \\ &- \sum_{i=1, i\neq k}^{M} \omega_{ik} \cdot g\left\{P_{ik}\Lambda_{ik}^{-1}P_{ik}^T[G(\Psi_i - \Psi_k) - \bar{\Delta}_{i,k}]\right\} \\ &-\omega_{kk} \cdot g\left\{U_k\Sigma^{-1}U_k^T[G(\Psi_k - \bar{\Psi}_k)]\right\} \end{aligned} \quad (5)$$

To simplify the complexity of the segmentation system, we generally choose the parameters in our experiments as follows: $\omega_{ik} = \omega_{kk} = \omega_k$, $\lambda_{1k} = \lambda_{2k} = \lambda_k = 1 - \omega_k$, $\mu_k = 0.00005 \cdot 255^2$, $\nu_k = 0$ [38]. This leaves us only one free parameter (ω_k) to balance the influence of two terms: the image data term and the neighbor prior term for each object. G denotes the conversion from a matrix to a vector by column scanning. g is the inverse of G. The trade-off between neighbor prior and image information depends on how much faith one has in the neighbor prior model and the image-derived information for a given application. We set these parameters empirically given the image quality and the neighbor prior information.

Experiments and Results In extensive testing using simulated image data, we have found that using the shape prior alone reduced the final er-

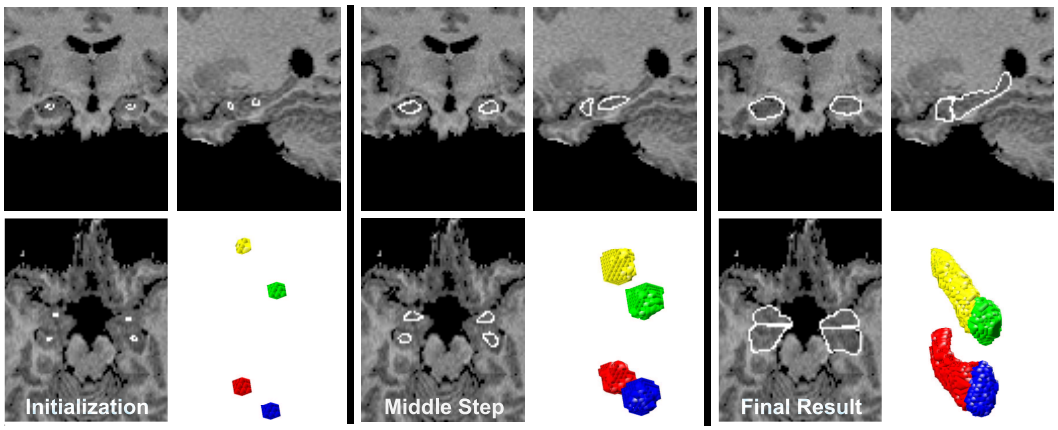

Fig. 4. Stages in the simultaneous segmentation of both the left and right amygdalae and hippocampi from a T1-weighted 3D MR brain image. Included with permission. $\lambda_k = 0.1$, $\omega_k = 0.9$, $k = 1, 2, 3, 4$.

ror in the presence of varying noise and surface seed initialization, but the addition of the neighbor prior always reduced the segmentation errors limiting them to a very small range even for large noise variance and for varying seed points [41,31].

To illustrate the utility of our neighbor-constrained approach to segment a particular neuroanatomical structure of interest to us, we have applied it to the segmentation of the left and right amygdalae and the left and right hippocampi, structures of particular interest in autism. Note that here, contralateral structures provide context due to the strong bilateral symmetry in the brain. In this work, we compared the results of our fully automated, neighbor-constrained segmentations to slice-by-slice manual tracings of the same structure, using a set of N=12 rigidly pre-aligned normal male subjects with an age range of 14 to 43. Note that even a relatively small sample provides a valuable constraint for images of subjects in the same population group. These 3D anatomical MR images have $(1.2 \text{ mm})^3$ resolution. Prior distributions for the automated algorithm were created for each test subject using a leave-one-out approach, where both the self-shape/size priors on any one object (e.g. the left amygdala) and neighboring-objects (e.g. right amygdala, left/right hippocampi) priors are found from manual tracings of these structures on the other 11 test images. The initial training data were found from twelve 3D MRI structural T1-weighted images. Thus, using the any one object to key on, we assumed it was independently related to the other 3 structures. Using PCA, we built the object self shape/size model of each object and the neighbor difference models between it and the other three structures. In this initial work, we used additional regularizing terms in the formulation of the objective function (different for each object), one to enforce smooth boundaries and one a scalar term related to the approximate volume of the object.

One of the results of running our neighbor-constrained MAP algorithm on a

Subject #	1	2	3	4	5	6	7	8	9	10	11	12	Mean	Std.
l. amygdala	1.6	1.2	1.3	0.9	1.5	1.5	1.4	1.3	1.0	1.5	1.2	1.4	1.32	0.21
r. amygdala	1.4	1.4	1.5	1.1	1.1	1.2	1.6	1.5	1.1	1.3	1.2	1.4	1.32	0.17
l. hippocampus	1.8	1.9	1.8	1.7	1.9	2.1	1.9	2.0	1.6	2.3	1.9	1.7	1.88	0.19
r. hippocampus	2.1	2.2	1.7	1.9	1.7	1.9	2.0	1.7	1.8	2.0	2.1	1.9	1.92	0.17

Table 1
Average distance between the computed and the manually-traced boundaries of the left and right amygdala and hippocampus for 12 subjects (in mm). Std.: standard deviation.

anatomical MR image using manually-traced priors is shown in Figure 4. We report the errors of the application of this algorithm on a set of 12 subjects in Table 1. The mean and standard deviation for each structure over the 12 subjects are also shown in Table 1. Virtually all the boundary points lie within one or two millimeters of the manual segmentation. Note that we have begun to extend this approach with the inclusion of coupled intensity-appearance/shape priors [68].

4 Tracking White Matter Fiber Pathways from DTI

As part of our overall approach to structural brain analysis, we have been actively investigating the use of a wavefront/level set-based strategies to estimate white matter fiber connectivity in the human brain [69]. In this work, we first employ an anisotropic version of the static Hamilton-Jacobi equation, and solve it by a sweeping method in order to obtain accurate front arrival times and determine connectivity. We briefly describe each part of this strategy below and present some early results as well.

Overview of Approach White matter connectivity can be viewed as an instance of the minimum-cost path problem in an oriented weighted domain. One would like to find a fiber path that minimizes the cumulative travel cost from a starting point A to some destination point B in the white matter. Because of the directionality of the tensor field, the cost function, τ, or its reciprocal speed $F = 1/\tau$, is anisotropic, as it is a function of both position $P(s)$ and direction $P'(s)$. The minimum cumulative cost at x is defined as:

$$T(x) = \min_{P} \int_{0}^{L} \tau(P(s), P'(s))\, ds \tag{6}$$

where L is pathway length, and the starting and ending points are given by $P(0) = A$ and $P(L) = x$. A solution to Equation 6 also satisfies the wave propagation equation:

$$\|\nabla T\| = \tau\,(x, \nabla T) \tag{7}$$

which describes a wavefront propagating with speed $1/\tau$. In continuous space, solutions to Equation 7 are given by the Hamilton-Jacobi (HJ) equations. While a classical solution to Equation 7 may not exist, the viscosity solution is commonly sought using numerical approximations [70–72].

Once the evolution equation (7) is solved for all points in the domain, one can use the resulting arrival times and find a solution for Equation 6. The minimum-cost path between point A and an arbitrary point B in the white matter then becomes a solution to:

$$\frac{dX}{dt} = -\nabla T \tag{8}$$

given $X(0) = B$. This optimal path can be constructed by integrating Equation 8 at point B back to the seed point A using standard techniques.

In order to trace connectivity in the white matter, we use the entire tensor in our propagation model to avoid the possible misclassification of the principal eigenvector in oblate tensor regions, which may lead to wrong assignment of front arrival times. We design our wavefront to evolve from a seed point A, $T(A) = 0$, at a speed governed by a function of the diffusivity magnitude d in the front normal direction $\vec{n}$:

$$\|\nabla T\| \cdot F(d(\vec{n})) \;=\; 1, \tag{9}$$

where F is designed to be large for large diffusivity and to slow the front rapidly when the diffusivity decreases. In addition, F accounts for the local anisotropy in order to stop the front from advancing into areas such as the ventricles or gray matter. In this way, we let the speed vary locally according to the tensor profile, descriptive of the underlying tissue structure.

The propagation equation belongs to a family of static Hamilton-Jacobi equations described by:

$$H(x, \nabla T) = V(x), \quad T(x) = q(x) \qquad x \in \Omega \tag{10}$$

where Ω is the domain in $\mathbb{R}^3$, $V(x) = 1$, and $q(x)$ is a function prescribing boundary condition values, $T(A) = q(A) = 0$. While the propagation equation

can be reformulated as a time-dependent HJ equation and solved by recovering each zero-level set, it is more convenient and less computationally expensive to model it as a static problem and determine arrival times instead.

Hamiltonians such as these cannot be correctly solved by isotropic propagation methods. However, carefully crafted methods have been devised [70–72] to construct accurate solutions for anisotropic equations. We use a Lax-Friedrichs (LF) discretization of our Hamiltonian and employ a nonlinear Gauss-Seidel updating scheme [71] to solve the propagation equation. No minimization is required when updating an arrival time, and thus it is very easy to implement. Details on the LF sweeping (LFS) scheme can be found in Kao *et al.* [71].

Experiments and Results Fig. 5a shows a synthetic model consisting of two fiber bundles, A and B, oriented along helical paths which cross each other at their middle section. The background was filled with nearly isotropic tensors. and diffusion-weighted images were created with added Gaussian noise. The signal-to-noise ratio is roughly half what is encountered in real diffusion MR scans, considering a single acquisition average. Fig. 5b depicts a close-up of the fiber-crossing region where oblate tensors resulting from the crossing are found. Streamlining techniques fail in such regions because of the oblate tensors in the fiber crossing region. Using our method, we reconstructed the pathways properly without deviating the fiber trajectories. One of the resulting tensor images is shown in Fig. 5c. A seed point A_1 was fixed at the bottom of bundle A (Fig. 5c) and our wavefront (γ=2) was propagated using the LFS method on the tensor images. Points A_2, B_1 and B_2 were fixed at the extreme ends of each bundle (Fig. 5c) and corresponding pathways A_2A_1, B_1A_1 and B_2A_1 were traced on ∇T images using a Runge-Kutta 4^{th}-order integration. Fig. 5d illustrates the resulting connectivity pathways embedded in the arrival time images and corresponding arrival isocurves (up to time 100). Darker areas in the maps show earlier arrivals. The fiber crossing region did not prevent pathways connecting different branches or the same branch (A_2A_1) from being recovered. To assess the variability of the extracted paths, we propagated the same front in the diffusion tensor image without added noise and then computed the mean distance between corresponding pathways. The mean distance for all paths under noise $\sigma^2 = 0.05$ was 1.06 voxels; for $\sigma^2 = 0.15$, was 1.22 voxels; and for $\sigma^2 = 0.20$, was 1.65 voxels. At the intersection, the maximum distance to the original pathway under noise variance $\sigma^2 = 0.20$ was an average of 1.34 pixels. The largest errors, an average of 2.67 pixels, occurred not at the intersection itself, but rather in the remaining trajectories after propagating through the crossing. We attribute this deviation to the added noise in the region of the intersection, thereby altering the original trajectory. Nonetheless, the recovered pathways remained close to their original trajectories in spite of the added noise. Variations in the seed point location (A_1) result in different pathway solutions, depending on the local tensor field directionality.

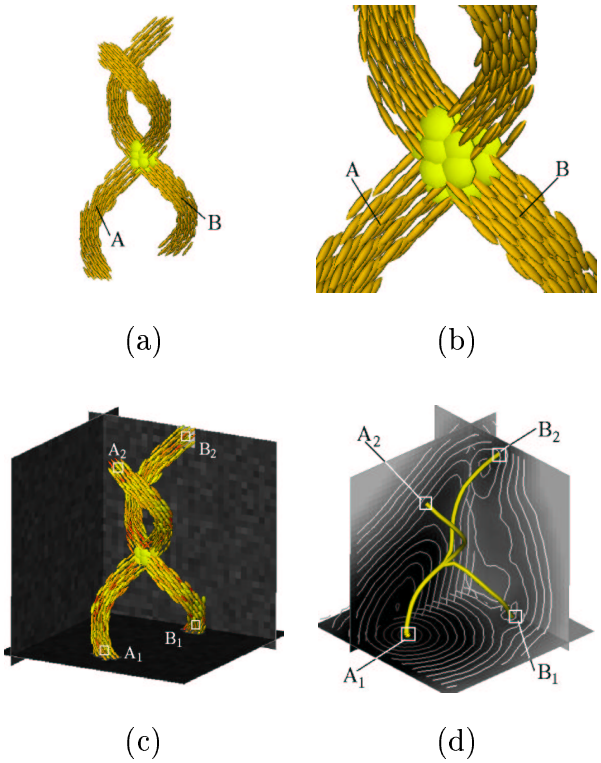

(a) (b)

(c) (d)

Fig. 5. (a) Synthetic dataset containing two fiber bundles with main diffusivities $\{9, 2, 1\}$ mm^2/s. (b) Close-up of the fiber-crossing and resulting oblate tensors. (c) Example tensor model with additive Gaussian noise (0.15) (d) Corresponding times of arrival and connectivity pathways.

We applied our method on real human data, fixing the seed point in the splenium of the corpus callosum (Fig. 6a). We then propagated our wavefront throughout the image using the LFS method. Fig. 6a depicts the resulting arrival time level sets between 0 and 500. All pathways between points on the white matter boundary and the point in the splenium were traced using the map of arrival times. Fig. 6b shows the resulting 20,817 pathways, colored by the fractional anisotropy at each point, where brighter points represent higher anisotropy. Thus, we can observe the main routes of connection between various brain regions and the splenium. Not all connections shown in Fig. 6 represent true anatomical pathways. In future work, we will incorporate a metric to rate their anatomical likelihood.

5 Nonrigid Brain Registration Using Extended Robust Point Matching for Composite Multisubject Analysis

We have developed a method that builds on and extends the robust point matching framework (RPM) previously developed by our group [73,63]. RPM was originally presented in the context of joint estimation of rigid trans-

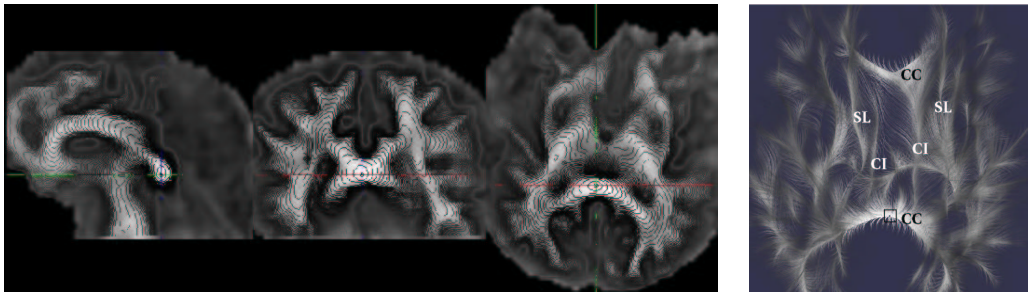

(a) (b)

Fig. 6. (a) Level sets depicting arrival times between 0 and 500, after propagation using the LFS method. (b) Close-up view of the main pathways connecting to the splenium. Points leaving the genu of the corpus callosum (CC) connect to the splenium via the cingulum (CI) pathways, and points in the superior frontal lobe connect via the superior longitudinal fasciculi (SL), consistent with known anatomy.

formations (affine and piecewise-affine) and correspondences using "softassign" and deterministic annealing [74]. Developed in an optimization framework, this previous work models point matching as a linear assignment–least squares problem. The algorithm estimates fuzzy correspondences while enforcing the one-to-one constraint. A deterministic annealing optimization framework gradually reduces the fuzziness of the correspondence in a controlled manner. Progressively refined transformation parameters are estimated by the resulting alternating update algorithm. The framework was first extended to the non-linear registration case by Chui *et al.* [75], and was evaluated on a synthetic data-set as has been reported [73,63]. The algorithm was shown to map landmarks to an accuracy of the order of 1-2.5 mm on average, which is superior to the typical performance of intensity based methods in the cortex [59]. However, this algorithm was hampered by (a) the limitation to a relatively small number of points and (b) the lack of outlier rejection, as a result of a clustering scheme used to increase the actual number of points.

As we have reported [76], we have extended the robust point matching algorithm to address both of these issues. We explicitly use the measure of "outlierness" estimated in the correspondence stage of this algorithm as a weight in the transformation estimation step to account for outliers in the template. Advanced numerical and graphics techniques such as sparse matrices and proper search strategies are also employed to enable the algorithm to use large numbers of points, which is important in the context of nonrigid brain registration.

Extended RPM: An Overview We present here a modified form of the standard RPM methodology [63]. The registration procedure consists of two alternative steps: (i) the correspondence estimation step and (ii) the transformation estimation step. In the following discussion, we label the reference

point set as X and the transform point set as Y. The goal of the registration is to estimate the transformation $G : X \mapsto Y$. We label G^k the estimate of G at the end of iteration k. G^0 is the starting transformation which can be the identity transformation. The whole process is embedded in a deterministic annealing framework, where the temperature T is progressively lowered, gradually decreasing the fuzziness of the correspondence and the smoothness of the transformation.

(i) Correspondence Estimation: Given the point sets X and Y, we estimate the match matrix M, where M_{ij} is the distance metric between points $G^k(X_i)$ and Y_j. The standard distance metric is defined as:

$$M_{ij} = \frac{1}{\sqrt{2\pi T^2}} e^{\frac{-|G^k(X_i) - Y_j|^2}{2T^2}} \tag{11}$$

$$\forall i \; : \; \sum_j M_{ij} + C_i = 1 \tag{12}$$

$$\forall j \; : \; \sum_i M_{ij} + R_j = 1 \tag{13}$$

where $|X_i - Y_j|$ is the Euclidean distance between points X_i and Y_j and T is the temperature term that controls the fuzziness of the correspondence. Further, we restrict the correspondences to resemble a linear assignment problem – this requires that the rows and columns of M must sum to 1. In order to handle outliers, we introduce an outlier column C and an outlier row R, where C_i is a measure of the degree of "outlierness" of a point in the reference point set X_i and R_j is the same for a point in the transform point set Y_j. C and R are initialized with constant values and then, using an iterative procedure [77], the values of M, C and R are normalized to satisfy equations 12 and 13.

Once the normalization is completed, we can compute the corresponding points as follows. Let V_i be the corresponding point to X_i and w_i the confidence in the match. Then V_i is defined as a normalized weighted sum of the points Y_j where the weights are the elements of the match matrix M.

$$w_i = (\sum_j M_{ij}) = 1 - C_i, \quad \text{and } V_i = \frac{1}{w_i} \sum_j M_{ij} Y_j \tag{14}$$

Note that a point that has a high value in the outlier column C will have low confidence and vice-versa.

(ii)Transformation Estimation: The transformation is estimated simply using

a regularized weighted least squares fit between X_i and V_i as follows:

$$G^k = \arg\min_g \sum_i w_i (g(X_i) - V_i)^2 + f(T)\mathcal{S}(g) \tag{15}$$

where $\mathcal{S}(g)$ is a regularization functional (e.g. a bending energy function) weighted by a function of the temperature, $f(T)$. This last weighting term is used to decrease the regularization as we approach convergence.

Registration Accuracy on a group of normal controls As an initial evaluation of the methodology, we tested it on a set of magnetic resonance 3D SPGR images, with isotropic $(1.2 \text{ mm})^3$ voxels, acquired using a GE 1.5 T scanner on a sample of 39 normal male controls (age 23.5 ± 10.2, IQ in the average range). We segmented the gray matter using our coupled level set algorithm [20] that was described earlier. Next, the gray matter ribbon surrounding the fusiform gyri was isolated using manual tracing and points from the gray matter surfaces were extracted and used as an input to our extended RPM algorithm [76], together with points from the cortical surfaces. Nonrigid registration using RPM to a separate normal template brain image yielded a transformation parameterized as a dense displacement field. An analysis of the registration results showed that the average errors were (a) 1.1 mm for points on the outer cortical surface and (b) 1.4 mm for points on the fusiform surfaces. These errors were determined by computing the distance from points on the warped reference surface to the corresponding points on the target surface, thus ensuring one-to-one correspondences.

Tensor-based Morphometric Study of Williams Syndrome To illustrate the utility of the approach, we performed a tensor-based morphometric study of the structural differences between normal controls and Williams syndrome subjects. Jackowski *et al.* [78,79] previously reported that the distances between the ends of the central sulci and the midline were larger in Williams patients compared to normal controls once total brain size was factored out. In collaboration with the authors of this study, we attempted to reproduce this finding using our point based registration method.

In this work, 3D SPGR magnetic resonance images with isotropic $(1.2 \text{ mm})^3$ voxels were acquired using a GE 1.5 T scanner on a sample of 27 Williams syndrome subjects and 20 controls (groups were matched in terms of gender and age). We manually traced the superior frontal sulci and the central sulci (as reported in Jackowski *et al.* [78,79]) which were used as inputs to our extended RPM algorithm [76], together with points from the cortical surfaces, registering to a normal template image.

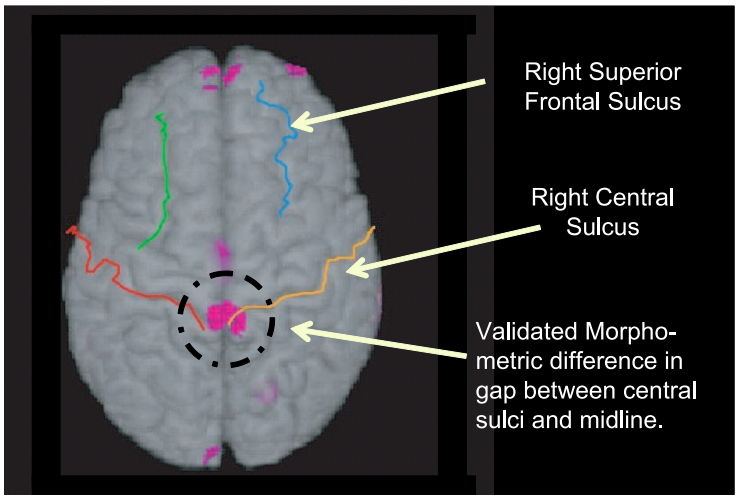

Fig. 7. Composite Jacobian map derived using extended RPM applied to 27 Williams subjects and 20 controls showing significance ($p < .001$). Extended RPM using the brain surface and the four sulci indicated yields significant structural differences in the region between the central sulci replicating a previously observed structural difference (Colorscale: Purple/Blue: Williams > Controls).

A tensor-based deformation measure (the determinant of the Jacobian of the displacement field) was computed from the displacement field to provide a quantitative metric of the local expansion/contraction needed for each voxel to register to the template. The deformation measure was sampled every 1.5 mm and smoothed (FWHM = 3.1 mm), and groups were then compared by creating a t-map (adjusted for overall brain size scaling differences) keeping all values more significant than $p < .001$ (uncorrected). Differences shown on the t-map away from the sulci may not be reliable since sulcal points were not used there to define local anatomy. However, as shown in Figure 7, and in accordance with the earlier reported finding, we observe a bilateral morphometric difference between the ends of the central sulci and the midline. We note that using an intensity based non-linear registration yielded less significant differences only in the left hemisphere as a result of inaccuracies in the registration of the sulci.

While we believe the registration results near the regions of interest such as the central and superior frontal sulci are accurate, we feel that the results in other regions are more variable. To address this, we are currently working on an integrated feature/intensity nonrigid registration strategy [80].

6 Discussion

The reliable and accurate derivation of parametric information from structural MR images useful for quantifying differences related to a range of neuropsy-

chiatric disorders requires a number of stages of processing (some of which are not mentioned here). In this paper, we have described four related image analysis efforts aimed at the quantification of cortical and subcortical gray matter and white matter interconnections, along with a strategy for registering multiple subject structural image information. Our overall approach to these problems is to focus on different specific regions rather than attempting to analyze the entire brain at once. In this context, we have often found it advantageous to focus on methods that rely on Bayesian reasoning strategies that permit the incorporation of spatial relationship priors representing the geometrical/biological variability across a population. In addition, level set and wavefront propagation strategies, such as were used for subcortical and cortical segmentation, as well as for diffusion image analysis, have proven to be useful and generally robust methodologies for our purposes. Finally, we note that our registration strategy focuses on regionally-segmented structure, an approach that we have found useful in a variety of analyses. Our future directions are aimed at integrating functional and structural information within this same basic framework.

7 Acknowledgements

We would like to acknowledge the help of collaborators Robert Schultz, Andrea Jackowski and Todd Constable as well as the support of NIH-NINDS grant R01NS035193 and NIH-NIBIB grant R01EB000311.

References

[1] D. Geman, S. Geman, Stochastic relaxation, Gibbs distribution and the Bayesian restoration of images, IEEE Trans. Pattern Analysis and Machine Intelligence 6 (6) (1984) 721–741.

[2] R. Leahy, T. Hebert, R. Lee, Applications of Markov random fields in medical imaging, in: Information Processing in Medical Imaging, Wiley-Liss Inc, 1991, pp. 1–14.

[3] V. Barra, J.-Y. Boire, Automatic segmentation of subcortical brain structures in MR images using information fusion, IEEE Trans. Medical Imaging 20 (7) (2001) 549–558.

[4] W. M. Wells, W. Grimson, R. Kikinis, F. A. Jolesz, Statistical intensity correction and segmentation of MRI data, in: R. A. Robb (Ed.), Visualization Biomed. Comput. 1994, SPIE 2359, 1994, pp. 148–159.

[5] H. E. Cline, W. E. Lorensen, R. Kikinis, F. Jolesz, Three-dimensional segmentation of MR images of the head using probability and connectivity, J. Comp. Assisted Tomogr. 14 (6) (1990) 1037–1045.

[6] Z. Liang, R. F. Jaszczak, R. E. Coleman, Parameter estimation of finite mixtures using the EM algorithm and information criteria with application to medical image processing, IEEE Trans. Nucl. Sci. 39 (4) (1992) 1126–1133.

[7] M. Kass, A. Witkin, D. Terzopoulos, Snakes: Active contour models, International Journal of Computer Vision 1 (1988) 312–331.

[8] S. Osher, J. A. Sethian, Fronts propagating with curvature-dependent speed: Algorithms based on Hamilton–Jacobi formulations, J. Comp. Physics 79 (1988) 12–49.

[9] S. Osher, N. Paragios, Geometric Level Set Methods, Springer, New York, 2003.

[10] R. Malladi, R. Kimmel, D. Adalsteinsson, G. Sapiro, V. Caselles, J. A. Sethian, A geometric approach to segmentation and analysis of 3D medical images, in: Proc. Workshop Math. Meth. Biomed. Image Anal., 1996, pp. 244–252.

[11] R. Malladi, J. A. Sethian, B. C. Vemuri, Shape modeling with front propagation: A level set approach, IEEE Trans. Pattern Analysis and Machine Intelligence 17 (1995) 158–175.

[12] J. A. Sethian, Level set methods: Evolving interfaces in geometry, fluid mechanics, computer vision and materials science, Cambridge University Press, 1996.

[13] X. Han, C. Xu, J. L. Prince, A topology preserving level set method for geometric deformable models, IEEE Trans. Pattern Analysis and Machine Intelligence 25 (6) (2003) 755–768.

[14] C. A. Davatzikos, J. Prince, An active contour model for mapping the cortex, IEEE Trans. Medical Imaging 14 (1) (1995) 65–80.

[15] C. Xu, D. Pham, J. Prince, M. Etemad, D. Yu, Reconstruction of the central layer of the human cerebral cortex from MR images, in: Medical Image Computing and Computer Assisted Intervention, LNCS 1496, Springer, Berlin, 1998, pp. 481–488.

[16] P. C. Teo, G. Sapiro, B. A. Wandell, Creating connected representations of cortical gray matter for functional MRI visualization, IEEE Trans. Medical Imaging 16 (6) (1997) 852–863.

[17] D. MacDonald, D. Avis, A. C. Evans, Proximity constraints in deformable models for cortical surface identification, in: Medical Image Computing and Computer Assisted Intervention, LNCS 1496, Springer, Berlin, 1998, pp. 650–659.

[18] T. Kapur, W. Grimson, W. Wells, R. Kikinis, Segmentation of brain tissue from magnetic resonance images, Med. Image Anal. 1 (2) (1996) 109–128.

[19] L. H. Staib, X. Zeng, A. Chakraborty, R. T. Schultz, J. S. Duncan, Shape constraints in deformable models, in: I. Bankman (Ed.), Handbook of Medical Imaging: Processing and Analysis, Academic Press, San Diego, 2000, pp. 147–157.

[20] X. Zeng, L. H. Staib, R. T. Schultz, J. S. Duncan, Segmentation and measurement of volumetric layers using coupled surfaces propagation, IEEE Trans. Medical Imaging 18 (10) (1999) 927–938.

[21] M. Vaillant, C. A. Davatzikos, Finding parametric representations of the cortical sulci using an active contour model, Med. Image Anal. 1 (4) (1997) 295–315.

[22] X. Zeng, L. H. Staib, R. T. Schultz, J. S. Duncan, Segmentation and measurement of the cortex from 3D MR images, in: Medical Image Computing and Computer Assisted Intervention, LNCS 1496, Springer, Berlin, 1998, pp. 519–530.

[23] J.-P. Thirion, New feature points based on geometric invariants for 3D image registration, International Journal of Computer Vision 18 (2) (1996) 121–137.

[24] D. Collins, A. Evans, C. Holmes, T. Peters, Automatic 3D segmentation of neuro-anatomical structures from MRI, in: Y. Bizais, C. Barillot, R. D. Paola (Eds.), Information Processing in Medical Imaging, Kluwer, Dordrecht, 1995, pp. 139–152.

[25] J. Declerck, G. Subsol, J. Thirion, N. Ayache, Automatic retrieval of anatomical structures in 3D medical images, in: N. Ayache (Ed.), Comp. Vision, Virtual Reality and Robotics in Med. (CVRMed '95), LNCS 905, Springer-Verlag, Berlin, 1995, pp. 153–162.

[26] D. Collins, T. Peters, W. Dai, A. Evans, Model based segmentation of individual brain structures from MRI data, in: R. A. Robb (Ed.), Visualization Biomed. Comput. 1992, SPIE 1808, 1992, pp. 10–23.

[27] P. Thompson, D. MacDonald, M. Mega, C. Holmes, A. Evans, A. Toga, Detection and mapping of abnormal brain structure with a probabilistic atlas of cortical surfaces, J. Comp. Assisted Tomogr. 21 (4) (1997) 567–581.

[28] L. H. Staib, J. S. Duncan, Boundary finding with parametrically deformable models, IEEE Trans. Pattern Analysis and Machine Intelligence 14 (1992) 161–175.

[29] L. H. Staib, J. S. Duncan, Model-based deformable surface finding for medical images, IEEE Trans. Medical Imaging 15 (5) (1996) 720–731.

[30] Y. Wang, L. H. Staib, Boundary finding with correspondence using statistical shape models, in: Proc. Comp. Vision Pattern Recog., 1998, pp. 338–345.

[31] J. Yang, L. H. Staib, J. S. Duncan, Neighbor-constrained segmentation with deformable models, in: Information Processing in Medical Imaging, LNCS 2732, Springer, 2003, pp. 198–209.

[32] J. Yang, H. D. Tagare, L. H. Staib, J. S. Duncan, Segmentation of 3D deformable objects with level set based prior models, in: IEEE Int. Symp. Biomedical Imaging (ISBI), 2004, pp. 85–88.

[33] T. Cootes, A. Hill, C. Taylor, J. Haslam, The use of active shape models for locating structures in medical images, in: H. H. Barrett, A. F. Gmitro (Eds.), Information Processing in Medical Imaging, LNCS 687, Springer-Verlag, Berlin, 1993, pp. 33–47.

[34] G. Szekély, A. Kelemen, C. Brechbüler, G. Gerig, Segmentation of 3D objects from MRI volume data using constrained elastic deformations of flexible Fourier surface models, in: N. Ayache (Ed.), Comp. Vision, Virtual Reality and Robotics in Med. (CVRMed '95), LNCS 905, Springer-Verlag, Berlin, 1995, pp. 495–505.

[35] A. Chakraborty, L. H. Staib, J. S. Duncan, Deformable boundary finding in medical images by integrating gradient and region information, IEEE Trans. Medical Imaging 15 (6) (1996) 859–870.

[36] L. H. Staib, A. Chakraborty, J. S. Duncan, An integrated approach for locating neuroanatomical structure from MRI, Int. J. Patt. Recog. Art. Intell. 11 (8) (1997) 1247–1269, (Special Issue on MR Brain Image Analysis).

[37] A. Chakraborty, J. Duncan, Game theoretic integration for image segmentation, IEEE Trans. Pattern Analysis and Machine Intelligence 21 (1) (1999) 12–30.

[38] T. Chan, L. Vese, Active contours without edges, IEEE Trans. Image Proc. 10 (2) (2001) 266–277.

[39] M. Leventon, E. Grimson, O. Faugeras, Statistical shape influence in geodesic active contours, in: Proc. Comp. Vision Pattern Recog., 2000, pp. 316–323.

[40] V. Caselles, R. Kimmel, G. Sapiro, Geodesic active contours, International Journal of Computer Vision 22 (1997) 61–79.

[41] J. Yang, L. H. Staib, J. S. Duncan, Neighbor-constrained segmentation with level set based 3D deformable models, IEEE Trans. Medical Imaging (in press).

[42] A. Tsai, A. Yezzi, W. Wells, C. Tempany, D. Tucker, A. Fan, W. Grimson, A. Willsky, Model-based curve evolution technique for image segmentation, in: Proc. Comp. Vision Pattern Recog., 2001, pp. 463–468.

[43] A. Tsai, W. Wells, C. Tempany, E. Grimson, A. Willsky, Coupled multi-shape model and mutual information for medical image segmentation, in: C. Taylor, A. Noble (Eds.), Information Processing in Medical Imaging, LNCS 2732, Springer, Berlin, 2003, pp. 185–197.

[44] G. Gerig, M. Styner, M. E. Shenton, J. A. Lieberman, Shape versus size: Improved understanding of the morphology of brain structures, in: M. A. Viergever, T. Dohi, M. Vannier (Eds.), Medical Image Computing and Computer Assisted Intervention, LNCS 2208, Springer, 2001, pp. 24–32.

[45] P. J. Basser, C. Pierpaoli, Microstructural and physiological features of tissues elucidated by quantitative-diffusion-tensor MRI, J. Mag. Res., Series B 111 (3) (1996) 209–219.

[46] S. Mori, P. C. M. van Zijl, Fiber tracking: principles and strategies - a technical review, NMR in Biomedicine 15 (7-8) (2002) 468–480.

[47] S. Osher, R. Fedkiw, Level Set Methods and Dynamic Implicit Surfaces, 1st Edition, Springer-Verlag, New York, 2003.

[48] G. J. M. Parker, C. A. M. Wheeler-Kingshott, G. J. Barker, Estimating distributed anatomical connectivity using fast marching methods and diffusion tensor imaging, IEEE Trans. Medical Imaging 21 (5) (2002) 505–512.

[49] C. Lenglet, R. Deriche, O. Faugeras, Diffusion tensor magnetic resonance imaging: Brain connectivity mapping, Research Report 4983, INRIA (2003).

[50] L. O'Donnell, S. Haker, C.-F. Westin, New approaches to estimation of white matter connectivity in diffusion tensor MRI: Elliptic PDEs and geodesics in a tensor-warped space, in: Medical Image Computing and Computer Assisted Intervention, LNCS 2489, Springer, Berlin, 2002, pp. 459–466.

[51] J. Talairach, P. Tournoux, Co-planar Stereotaxic Atlas of the Human Brain, Thieme Medical Publishers, New York, 1988.

[52] J. C. Mazziotta, A. W. Toga, A. C. Evans, P. Fox, J. Lancaster, A probabilistic atlas of the human brain: Theory and rationale for its development, NeuroImage 2 (1995) 89–101.

[53] A. Toga, P. Thompson, Multimodal brain atlases, in: S. Wong (Ed.), Advances in Biomedical Image Databases, Kluwer Academic Press, Dordrecht, 1999, pp. 53–58.

[54] A. Goshtasby, L. H. Staib, C. Studholme, D. Terzopoulos, Nonrigid image registration: Guest editors' introduction, Comp. Vision and Image Understanding 89 (2-3) (2003) 109–113.

[55] J. P. W. Pluim, J. M. Fitzpatrick, Image registration, IEEE Trans. Medical Imaging 22 (11) (2003) 1341–1343.

[56] G. E. Christensen, M. I. Miller, M. W. Vannier, Individualizing neuroanatomical atlases using a massively parallel computer, Computer (1996) 32–38.

[57] D. Rueckert, L. Sonoda, C. Hayes, D. Hill, M. Leach, D. Hawkes, Nonrigid registration using free-form deformations: application to breast MR images, IEEE Trans. Medical Imaging 18 (8) (1999) 712–721.

[58] K. J. Friston, J. Ashburner, J. B. Poline, C. D. Frith, J. D. Heather, R. S. J. Frackowiak, Spatial registration and normalization of images, Human Brain Mapping 2 (1995) 165–189.

[59] P. Hellier, C. Barillot, I. Corouge, B. Gibaud, G. Le Goualher, D. Collins, A. Evans, G. Malandain, N. Ayache, G. Christensen, H. Johnson, Retrospective evaluation of inter-subject brain registration, IEEE Trans. Medical Imaging 22 (9) (2003) 1120–1130.

[60] D. L. Collins, G. Le Goualher, A. C. Evans, Non-linear cerebral registration with sulcal constraints, in: Medical Image Computing and Computer Assisted Intervention, LNCS 1496, Springer, Berlin, 1998, pp. 974–984.

[61] C. A. Davatzikos, Spatial transformation and registration of brain images using elastically deformable models, Comp. Vision and Image Understanding 66 (2) (1997) 207–222.

[62] I. Corouge, C. Barillot, P. Hellier, P. Toulouse, B. Gibaud, Non-linear local registration of functional data, in: M. A. Viergever, T. Dohi, M. Vannier (Eds.), Medical Image Computing and Computer Assisted Intervention, LNCS 2208, Springer, 2001, pp. 948–956.

[63] H. Chui, L. Win, R. T. Schultz, J. S. Duncan, A. Rangarajan, A unified non-rigid feature registration method for brain mapping, Medical Image Analysis 7 (2) (2003) 113–130.

[64] Brainweb, McConnell Brain Imaging Center, Montreal Neurological Institute (MNI), Montreal, Quebec, http://www.bic.mni.mcgill.ca/brainweb/.

[65] Internet Brain Segmentation Repository, Center for Morphometric Analysis, Massachusetts General Hospital: http://www.cma.mgh.harvard.edu/ibsr/.

[66] X. Zeng, L. H. Staib, R. T. Schultz, H. Tagare, L. Win, J. S. Duncan, A new approach to 3D sulcal ribbon finding from MR images, in: Medical Image Computing and Computer Assisted Intervention, LNCS 1679, Springer, Berlin, 1999, pp. 148–157.

[67] J. Yang, L. H. Staib, J. S. Duncan, Statistical neighbor distance influence in active contours, in: Medical Image Computing and Computer Assisted Intervention, LNCS 2489, Springer, Berlin, 2002, pp. 588–595.

[68] J. Yang, J. S. Duncan, 3D image segmentation of deformable objects with shape appearance joint prior models, in: Medical Image Computing and Computer Assisted Intervention, Vol. 1, LNCS 2879, Springer-Verlag, 2003, pp. 573–580.

[69] M. Jackowski, C. Y. Kao, R. T. Constable, M. Qiu, L. H. Staib, Estimation of anatomical connectivity by anisotropic wave propagation and diffusion tensor imaging, in: Medical Image Computing and Computer Assisted Intervention, 2004.

[70] C. Kao, S. Osher, Y.-H. Tsai, Fast sweeping methods for static Hamilton-Jacobi equations, Technical Report, Math. Dept. 02-66, University of California, Los Angeles, ftp://ftp.math.ucla.edu/pub/camreport/cam02-66.pdf (2002).

[71] C. Kao, S. Osher, J. Qian, Lax-Friedrichs sweeping scheme for static Hamilton-Jacobi equations, Technical Report, Math. Dept. 03-38, University of California Los Angeles, Los Angeles, ftp://ftp.math.ucla.edu/pub/camreport/cam03-38.pdf (2003).

[72] J. A. Sethian, A. Vladimirsky, Ordered upwind methods for static Hamilton-Jacobi equations, Proceedings of the National Academy of Sciences USA 98 (20) (2001) 11069–11074.

[73] H. Chui, L. Win, R. Schultz, J. Duncan, A. Rangarajan, A unified feature registration method for brain mapping, in: M. Insana, R. Leahy (Eds.), Information Processing in Medical Imaging, 2001, pp. 300–314.

[74] A. Rangarajan, H. Chui, E. Mjolsness, S. Pappu, L. Davachi, P. Goldman-Rakic, J. Duncan, A robust point matching algorithm for autoradiograph alignment, Medical Image Analysis 4(1) (1997) 379–398.

[75] H. Chui, A. Rangarajan, New algorithm for non-rigid point matching, in: Proc. Comp. Vision Pattern Recog., Vol. 2, IEEE Press, Los Alamitos, CA, USA, 2000, pp. 44–51.

[76] X. Papademetris, A. P. Jackowski, R. T. Schultz, L. H. Staib, J. S. Duncan, Computing 3D non-rigid brain registration using extended robust point matching for composite multisubject fMRI analysis, in: Medical Image Computing and Computer Assisted Intervention, Vol. II, LNCS 2879, Springer-Verlag, 2003, pp. 788–795.

[77] A. Rangarajan, H. Chui, F. L. Bookstein, The Softassign Procrustes matching algorithm, in: J. S. Duncan, G. Gindi (Eds.), Information Processing in Medical Imaging, Springer, Berlin, 1997, pp. 29–42.

[78] A. P. Jackowski, R. T. Schultz, Brain morphology in Williams syndrome, in: 9th International Conference on Functional Mapping of the Human Brain, June 19-22, 2003, New York, NY, 2003, available on CD-Rom in NeuroImage 19(2).

[79] A. P. Jackowski, R. T. Schultz, Foreshortened dorsal extension of the central sulcus in Williams syndrome, Cortex, Special Issue on the Neurobiology of Developmental Disorders (in press).

[80] X. Papademetris, L. H. Staib, A. P. Jackowski, L. Y. Win, R. T. Schultz, J. S. Duncan, Integrating intensity and feature nonrigid registration, in: Medical Image Computing and Computer Assisted Intervention, 2004.